



Composition engineering to enhance the photovoltaic performance and to prolong the lifetime for silver bismuth iodide solar cell

Ming-Chung Wu^{a,b,c,*}, Qian-Han Wang^a, Kai-Chi Hsiao^a, Shih-Hsuan Chen^a, Ching-Mei Ho^a, Meng-Huan Jao^a, Yin-Hsuan Chang^a, Wei-Fang Su^{d,e}

^a Department of Chemical and Materials Engineering, College of Engineering, Chang Gung University, Taoyuan 33302, Taiwan

^b Green Technology Research Center, Chang Gung University, Taoyuan 33302, Taiwan

^c Division of Neonatology, Department of Pediatrics, Chang Gung Memorial Hospital at Linkou, Taoyuan 33305, Taiwan

^d Department of Materials Science and Engineering, National Taiwan University, Taipei 10617, Taiwan.

^e Department of Materials Engineering, Ming Chi University of Technology, New Taipei City 24301, Taiwan

ARTICLE INFO

Keywords:

Rudorffite
Solar cell
Silver bismuth iodide
Lead-free
Composition engineering, stability

ABSTRACT

Lead, a toxic element in organometal halide perovskite solar cells, has caught lots of attention and has raised public concerns after such perovskite solar cells made rapid progress in their photovoltaic performance. Herein, a series of lead-free light absorber layers with a rudorffite structure were examined in this study. The obscure role of A-site and B-site cation in silver bismuth iodide rudorffite materials has been revealed through their energy diagrams and surface potential analyses. By manipulating the stoichiometric ratio of bismuth and silver at a ratio of 1.1/3, a Ag₃BiI₆ layer with uniform morphology, high carrier mobility, and a high light response was obtained. The superior optoelectrical properties of the modified Ag₃BiI₆ active layer directly influenced the photovoltaic performance and the environmental stability of such a device. The photovoltaic device with the modified Ag₃BiI₆ active layer exhibited a PCE of 2.60%. It also maintained over 80% of its initial PCE after being stored in an ambient environment for over 3,000 h. This result sheds light on how to process silver bismuth iodide materials and extends the knowledge for rudorffite materials.

Introduction

Solution-processible lead halide perovskite solar cells have caught lots of attention since they first emerged in the last decade. Among several candidates, organo-lead halide perovskite (OLHP) has delivered sky-rocketed progress in photovoltaic performance. Efforts such as morphology controlled through anti-solvent engineering, stoichiometric manipulation, and evaporation processing of reactants have been developed to optimize deposition of OLHPs and to further promote the photovoltaic performance of perovskite solar cells [1–3]. The unprecedented photoconversion efficiency (PCE) of solar cells with OLPH as active layers has climbed to over 25%, which holds the highest PCE from thin-film photovoltaics in 2021.[4] Typically, an OLHP material can be depicted by the chemical formula of ABX₃. The divalent B-site cation is usually the lead ion, constructing a BX₆ octahedron with the B-site cation occupying the center and the six monovalent X-site anions, typically halide, occupying the corners. A monovalent organic molecule, such as methylammonium, formamidinium, or cesium, occupies the

center of the framework established by eight BX₆ octahedrons.[5] Taking advantage of optoelectrical properties, OLHPs are widely applied in photovoltaics, low dimensional materials of quantum dot, X-ray detection, and phototransistor applications.[6–9]

However, due to the raising awareness of environmental sustainability, the high toxicity and potential leakage of lead from organo-lead halide perovskite solar cells (OLHPSCs) become a concern for such photovoltaic technology for being applied into our daily life.[10, 11] Therefore, many efforts have been devoted to reducing or replacing the toxic element lead in OLHP materials.[12, 13] When considering the chemical properties, tin is the first candidate researcher have in mind to replace lead.[14–16] Tin share similar chemical properties and ionic radius with lead that helps it fit in the B-site of the perovskite structure. The promising PCE of 5.73% was obtained with a lead-free light-harvesting layer of methylammonium tin trihalide.[17] Yet, the preferred oxidization state of Sn⁴⁺ makes Sn-based perovskite photovoltaics exhibit inferior long-term stability due to the ease of Sn²⁺ ion oxidation in the ambient environment.[18–20] Also, the influences of Sn

* Corresponding author: Ming-Chung Wu, Phone, +886 3 2118800 #5771; Fax, +886 3 2118800 #53.

E-mail address: mingchungwu@cgu.edu.tw (M.-C. Wu).

<https://doi.org/10.1016/j.cej.2022.100275>

Available online 19 February 2022

2666-8211/© 2022 The Authors.

Published by Elsevier B.V. This is an open access article under the CC BY-NC-ND license

(<http://creativecommons.org/licenses/by-nc-nd/4.0/>).

on human health are still unclear. Therefore, all these factors restrict the development and of Sn-based perovskite photovoltaics. Bismuth-based material such as bismuth vanadate single crystal owing to its superior carrier density and conductivity has already been applied in photoelectrochemical water oxidation.[21]

To realize the concept of a lead-free light absorber layer, the silver bismuth iodide active layer has been studied owing to its relatively stable oxidation state and environmental tolerance.[22–24] Generally, the silver bismuth iodide compound is in the form of $\text{Ag}_x\text{Bi}_y\text{I}_z$, where $z = x + 3y$. $\text{Ag}_x\text{Bi}_y\text{I}_z$, abbreviated as SBI, exhibits a direct energy bandgap in the range of 1.70 to 1.85 eV and forms a similar crystal structure with the prototype oxide of NaVO_2 , namely ruderfite structure.[23, 25, 26] SBI ruderfite are three-dimensional structures constructed with a cubic close-packed iodide framework with cations of silver and bismuth occupying the edge-sharing octahedral position.[27] The relatively stable intrinsic property soon becomes an eye-catching material in the photovoltaic research community. Sargent's group is devoted to the improvement of film formation and morphology of SBI material in photovoltaics. Carboxyl amine of n-butylamine was first adopted as a solvent to dissolve and obtain a homogenous SBI precursor solution. The highest PCE achieved by the AgBi_2I_7 absorber was 1.22 %, with more than 10-days of ambient stability.[28] To manipulate and control the stoichiometry of silver iodide, whose solubility is highly dependent on temperature, a modified deposition of dynamic hot casting was reported to enlarge the grain size and obtain a pinhole-free Ag_2BiI_5 morphology. Taking advantage of dynamic hot casting, the solar cell based on the Ag_2BiI_5 active layer can deliver a higher photocurrent than it prepared from conventional deposition. The pinhole-free active layer facilitated carrier transportation and the corresponding device gained over 1.0% of PCE than the pristine one [29]. In addition to morphology modification, the energy level alignment between an active layer and carrier transporting layers and intrinsic optoelectronic property of an active layer play vital roles in the PCE of solar cells. Therefore, lots of attention focuses on the doping engineering of SBI or carrier transporting layers to enhance PCE. The anion in a semiconductor is believed to have a much stronger influence on the valence band than the conduction band. Therefore, to deal with the energy difference between the deep valence band edge of SBI and hole transporting layer, sulfide was adopted as a dopant to partially substitute iodide in SBI. The upward-shifted valence band of sulfide-doped SBI exhibited superior carrier-transfer ability and resulted in a PCE of 5.56%.[30] Thanks to the unoccupied d-orbital in copper, the conduction band edge of SBI materials can shift downward when copper is adopted as a dopant to partially replace silver in SBI. The modified conduction band of SBI improved its absorption ability as well as its carrier transferability. That resulted in an increased PCE from 2.04% to 2.53%.[31] Although many efforts have been devoted to the deposition and the doping engineering of SBI to promote their PCE, the information about composition engineering, especially for Bi cation, is still lacking. During the thermal-assisted crystallization of SBI, bismuth iodide (BiI_3) is likely to sublime or decompose from an as-casted thin film. The break of stoichiometric balance between silver and bismuth might adversely affect the ambipolar property in SBI active layer.

To manage the issue mentioned above, we focused on using ruderfite materials as the active layer to make a lead-free and air-stable photovoltaic. To realize the chemical composition effect between ruderfite structure and photovoltaic properties, a series of ruderfite materials including AgBi_2I_7 , AgBiI_4 , Ag_2BiI_5 , and Ag_3BiI_6 were prepared and discussed. Based on the examinations of light response surface potential change and light intensity-dependent I - V curve, Ag_3BiI_6 stood out from the series of ruderfite materials with relatively low defect density and minor trap-assisted recombination as it was struck by light. By manipulating the stoichiometry of BiI_3 , the desired SBI of Ag_3BiI_6 with an excess ratio of bismuth ($\text{Bi}/\text{Ag}=1.1/3$) exhibited pinhole-free surface morphology with high carrier mobility. The improved properties of the Ag_3BiI_6 active layer performed an average PCE of 2.23%, and the champion PCE achieved a PCE of 2.60%. In addition, the device with

ruderfite material exhibits an outstanding environmental tolerance. After being stored in an atmospheric environment for more than 3,000 hours (relative humidity of about 35%, 25°C), the corresponding device maintained more than 80% of the initial efficiency.

Results and discussion

All silver bismuth iodide ruderfite (SBI) materials were prepared with one-step deposition followed by an anti-solvent assisted crystallization step (detail see in Experimental section). To investigate the influences of Ag/Bi stoichiometry on either the structure or optoelectronic properties, a series of SBI materials including AgBi_2I_7 , AgBiI_4 , Ag_2BiI_5 , and Ag_3BiI_6 were prepared by manipulating the ratio of silver iodide and bismuth iodide. Notably, when constructing an SBI material, the states from Ag and Bi cation contribute differently to form orbital energy for either the valence band or the conduction band. It has been reported that the highest occupied energy of the valence band is mainly determined from the $4d$ orbital of silver and the $5p$ orbital of iodide. In contrast, the $6p$ orbital of bismuth contributes to forming the lowest occupied energy of the conduction band [32, 33]. Therefore, tuning the ratio of silver and bismuth is rational to manipulate both the energy level and energy bandgap of SBI materials. Fig. 1 demonstrates the energy bandgap (E_g) of various compositions of SBI thin films. The E_g of the AgBi_2I_7 thin film showed the lowest value, which can be ascribed to the high ratio of bismuth, in the series of SBI materials. The E_g of the others were slightly blue-shifted as the ratio of silver in SBI materials (*vide infra*) increased.

In addition to the bandgap of absorber layers, the band alignment in a photovoltaic device also plays a vital role in both carrier separation and carrier transfer. The potential difference between contacting layers triggers the photoexcited holes with a positive charge to transfer along with an electric field in a device. Whereas the photoexcited electrons with a negative charge transfer in the reversed direction. That helps to separate the photoexcited electron-hole pairs and promotes the quantum efficiency of devices. As a result, the correlation between the energy level, the energy bandgap, and the silver/bismuth ratio in SBI materials was further investigated using ultraviolet photoelectron spectroscopy (UPS). The results are shown in Fig. 2 (a), and the corresponding energy diagram was plotted in Fig. 2 (b). Silver, iodide and bismuth in SBI materials differently contribute to the formation energy level as constructed a ruderfite crystal structure. The $4d$ and $5p$ orbitals from silver and iodide mainly determine the minimum energy level of valence band. Whereas unoccupied $6p$ orbitals from bismuth in SBI materials affect the maximum energy level of conduction band.[32] When focusing on the energy level of AgBi_2I_7 materials, it exhibited the lowest band edge of the conduction band, which can be attributed to the dominant effect of antibonding from bismuth's $6p$ orbital and halide.[33] The low conduction band edge of AgBi_2I_7 might adversely affect the electron transition from its conduction band to the electron transport layer. As the ratio of bismuth was fixed in SBI materials, the highest occupied valence band of the SBI materials shifted upward when the ratio of silver increased. It has been reported that silver and iodide in SBI materials show a pronounced effect on their valence band due to the lower orbital energy of its $4d$ orbital.[33] The well-aligned energy level of devices with AgBiI_4 , Ag_2BiI_5 , and Ag_3BiI_6 absorber layers is speculated to facilitate the separation of the electron-hole pairs and harvest a higher photocurrent than those with inferior electron-hole pairs separation. The detailed information about energy level, energy bandgap, and work function of SBI materials from the UPS examination were summarized in Table 1.

Also, the contact potential difference (CPD), namely surface potential evolution, with on/off light illumination, was investigated to peer the carriers in SBI materials. The results are shown in Fig. 3 (a). The changed CPD of the absorber layers came from the electrons excited by photons with energy larger than E_g and resulted in the transition of electrons from the valence band to the conduction band. The created CPD was highly related to the response of light and the generation of

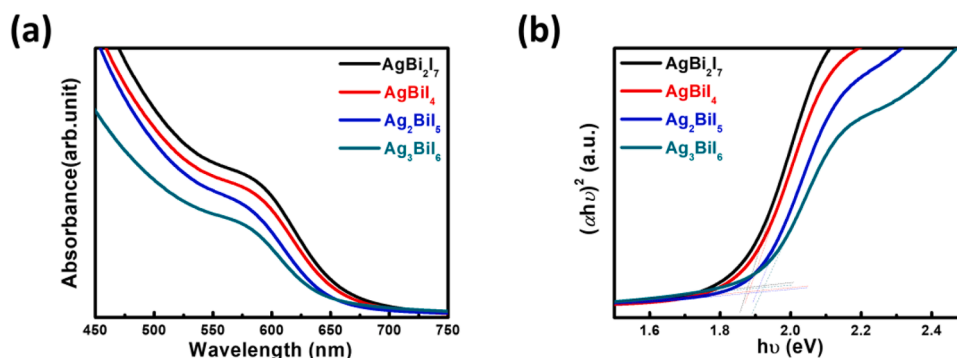


Fig. 1. Optical property for various ruddersite materials, including AgBi_2I_7 , AgBiI_4 , Ag_2BiI_5 , and Ag_3BiI_6 : (a) absorption spectra and (b) tauc plot for energy bandgap calculation.

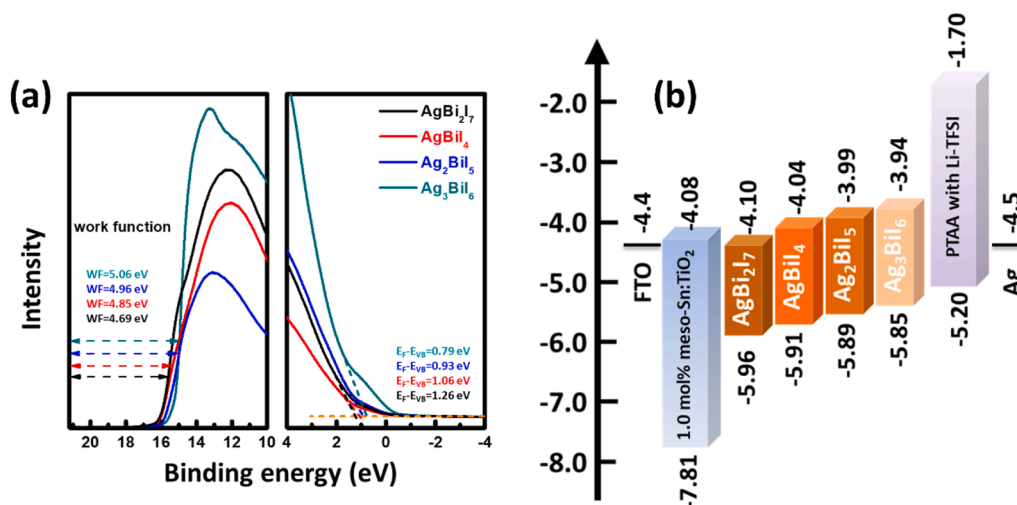


Fig. 2. Band structure analysis of various Ag/Bi ratio compositions: (a) ultraviolet photoelectron spectra and (b) band diagram of an entire device with various compositions of ruddersite materials.

Table 1

Bandgap, work function, and energy level of SBI absorber layers with various Ag/Bi ratios

Chemical composition	E_g (eV)	WF (eV)	E_{VB} (eV)	E_{CB} (eV)
AgBi_2I_7	1.86	4.69	-5.96	-4.10
AgBiI_4	1.87	4.85	-5.91	-4.04
Ag_2BiI_5	1.90	4.96	-5.89	-3.99
Ag_3BiI_6	1.91	5.06	-5.85	-3.94

electrons. Therefore, the greater the CPD evolution of SBI materials, the better the photovoltaic performance of the device is expected since more electrons are excited and transported to the conduction band. Fig. 3 (b) showed the photovoltaic performance of devices composed of various SBI materials. Ag_3BiI_6 exhibited the highest CPD evolution and PCE in the devices containing AgBi_2I_7 , AgBiI_4 , Ag_2BiI_5 , and Ag_3BiI_6 absorber layers.

Although the desired composition of silver bismuth iodide is achieved, bismuth is considered a volatile element due to its relatively low decomposing temperature and sublimating temperature.[34] Therefore, possible decomposition and sublimation of bismuth occur when the as-casted SBI film is held at a temperature of 150°C for annealing. Moreover, the decomposed or sublimated bismuth iodide adversely affects the surface morphology during the formation of SBI film. Yet, the annealing temperature also influentially affects crystallinity and crystal structure of SBI films. As a result, the series of Ag_3BiI_6 films with different annealing temperatures were examined by using X-ray

diffractometer. The results were shown in Fig. S1. According to Scherrer's equation as shown in followed, the grain size of SBI can be evaluated:

$$\tau = \frac{k\lambda}{\beta\cos(\theta)}$$

Here, τ implies grain size, k is the dimensionless shape factor, λ is the wavelength of incident X-ray, β is the line broadening at half the maximum intensity in radians, and θ is the Bragg's diffraction angle. For the characteristic peak at 13.27° that refer to plane (003) of Ag_3BiI_6 structure, the averaged grain size is 36.2 nm, 41.0 nm, 41.7 nm, and 36.3 nm for the films annealed at 120, 140, 160, and 180°C , respectively. The crystallinity of Ag_3BiI_6 film with annealing temperature at 160°C shows the largest grain size, which implies the highest crystallinity in the series, with the desired crystal structure of Ag_3BiI_6 . Therefore, the annealing temperature for SBI active layer was set at 160°C for further discussion.

To further investigate the relationship between properties of the SBI active layer and its resulting composition, the active layer of Ag_3BiI_6 , prepared from a stoichiometric ratio of $\frac{\text{BiI}_3}{\text{AgI}} = \frac{1}{3}$, was set as the standard active layer for further discussion. Manipulating the precursor of silver and bismuth ratio from the desired stoichiometric ratio ($\frac{\text{BiI}_3}{\text{AgI}} = \frac{1}{3}$) to the bismuth-rich precursor ($\frac{\text{BiI}_3}{\text{AgI}} > \frac{1}{3}$) is a possible path to counterbalance the loss of bismuth during the annealing process. As a result, the stoichiometric ratio of $\frac{\text{BiI}_3}{\text{AgI}}$ was manipulated to achieve the desired composition

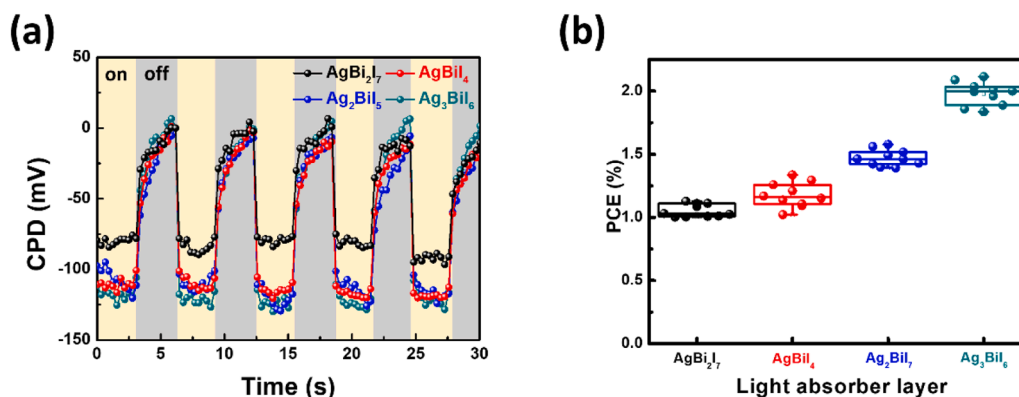


Fig. 3. Light response test for SBI with various stoichiometric ratios, including AgBi_2I_7 , AgBiI_4 , Ag_2BiI_5 , and Ag_3BiI_6 : (a) surface potential response under on-off illuminated condition and (b) PCE distribution of eight individual devices.

of the Ag_3BiI_6 active layer. The crystal structures of the active layers were first examined by using an x-ray diffractometer, and the results are shown in Fig. S2. The additional ratio of bismuth merely influenced the crystal structure, and all the active layers retained the desired ruddorffite structure of Ag_3BiI_6 . The optical properties of SBI with additional ratio of bismuth were shown in Fig. S3. Fig. 4 (a)~(e) demonstrated the surface morphology of Ag_3BiI_6 films from various stoichiometric ratios of the precursor defined as $\frac{\text{BiI}_3}{\text{AgI}} = \frac{(1+x)}{3}$. As the excess ratio of bismuth, x , increased from -0.1 to 0.5, the surface morphology changed gradually. For low excess ratios from -0.1 to 0.1, the surface of the SBI material contained precipitation of silver or silver iodide. The impurity of silver and its derivatives influenced the morphology of the SBI materials and increased the occurrence of pinholes in the active layers. As the excess ratio of bismuth further increased to larger than 0.1, the SBI materials formed large grains. However, the large grain size easily allowed the stacking grains to loosen and formed pores in the active layer. The pores in the active layer further led to the contact between the above carrier transporting layer and the beneath carrier transporting layer. That causes current leakage and deteriorates the photovoltaic performance of devices with such active layers ($x > 0.1$). The PV performance of devices composed of various active layers ($x = -0.1$ to 0.5) was summarized in Table S1. The above factors directly reflected on the PV performance of devices, and the devices with the excess ratio of $x = 0.1$ achieved an average PCE of 2.36%. The champion device improved the PCE from 2.10% ($x = 0.0$) to 2.60% ($x = 0.1$) as shown in Fig. S4. The progress of PCE was mainly contributed by the enhancement of current density, as

shown in Fig. S5. Although the morphology of the active layers gave us clear information about the progress of PCE, the unrevealed reasons of merely 30% of PCE enhancement still inspired us to explore the optoelectrical properties of the SBI materials. Considering the surface morphology and PV performance of devices with various SBI materials, the ratio of $\frac{\text{BiI}_3}{\text{AgI}} = \frac{1}{3}$, $x = 0.1$, was selected as the target active layer to discuss the relationship between optoelectrical properties and chemical composition.

For obtaining photovoltaics, the chemical composition and the surface morphology are the essential criteria for fabricating an active layer based on the macroscopic point of view. In comparison, the defects and carrier mobility in a photovoltaic device are crucial aspects of carrier transportation from the microscopic point of view. The Space-Charge Limit Current (SCLC) model is widely utilized to examine a semiconductor thin film's conductivity, trap density, and mobility. An I - V curve from either the electron-only or the hole-only structured device can be divided into three portions, including ohmic region ($I \propto V$), trap-filled limit region (TFL region, $I \propto V^n$, $n > 2$), and Child's region ($I \propto V^2$). According to the SCLC model, the transient point between the ohmic region and the trap-filled limit region is known as the trap-filled voltage (V_{TFL}). The relationship between the trap density in a film and V_{TFL} can be expressed using the following equation:

$$V_{TFL} = \frac{eN_t d^2}{2\epsilon\epsilon_0}$$

where e is the elementary charge, ϵ_0 is the dielectric constant in vacuum,

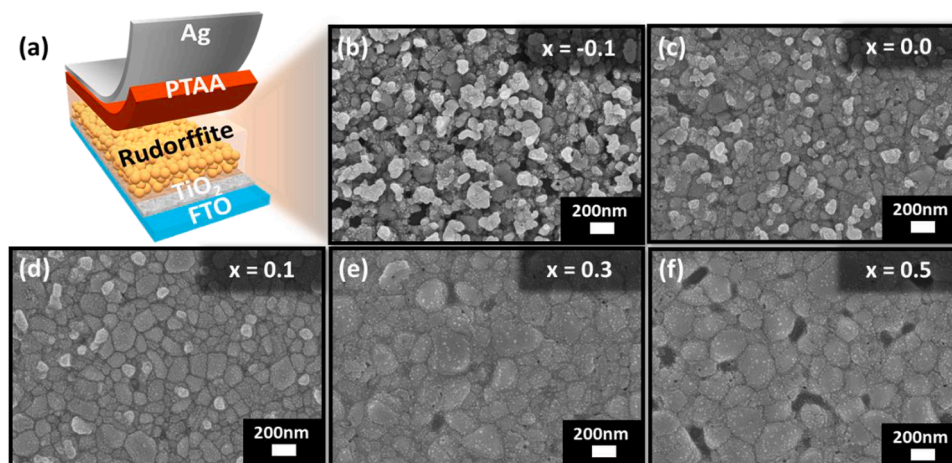


Fig. 4. Illustration of devices: (a) entire device with n-i-p architecture. Effect of various stoichiometric ratios of AgI and BiI_3 precursor solution on surface morphology of Ag_3BiI_6 thin films from: (b) $x = -0.1$, (b) $x = 0.0$, (c) $x = 0.1$, (d) $x = 0.3$, and (e) $x = 0.5$, where x indicates the excess bismuth indicated by $\frac{\text{BiI}_3}{\text{AgI}} = \frac{(1+x)}{3}$.

ϵ is the dielectric constant of SBI, which equals to 3.36, N_t is the trapped density, and d is the measured thickness of the thin film. The carrier mobility (μ) can also be acquired at the Child's region of the I - V curve using the Mott–Gurney law:

$$J = \frac{9\epsilon\epsilon_0\mu V^2}{8d^3}$$

The I - V curves based on the electron-only and the hole-only structured devices were demonstrated in Fig. 5 (a) and (c), respectively. The calculated electron and hole trap density and their mobility for Ag_3BiI_6 ($x=0.0$) and $\text{Ag}_3\text{Bi}_{1.1}\text{I}_{6.3}$ ($x=0.1$) active layers are shown in Table 2. It is noted that the trap density in an active layer is considered as either a recombination site or an annihilation site for carriers. Once the carriers are trapped, the carriers would process non-radiative recombination instead of transferring to the corresponding carrier transporting layers. That results in a low photocurrent in a device. When calculating the trap density in electron-only devices, N_t was found to be 2.21×10^{15} (number/cm³) for Ag_3BiI_6 active layer and 2.28×10^{15} (number/cm³) for $\text{Ag}_3\text{Bi}_{1.1}\text{I}_{6.3}$ active layer. Whereas in the hole-only devices, N_t was found to be 3.99×10^{14} (number/cm³) for Ag_3BiI_6 active layer and 3.63×10^{14} (number/cm³) for $\text{Ag}_3\text{Bi}_{1.1}\text{I}_{6.3}$ active layer. The similar trap densities for Ag_3BiI_6 and $\text{Ag}_3\text{Bi}_{1.1}\text{I}_{6.3}$ active layers indicated that the manipulation of AgI and BiI₃ reactants was slightly influential in the trap density in both the negative and the positive defects in the active layers. Surprisingly, mobility for both electron and hole in $\text{Ag}_3\text{Bi}_{1.1}\text{I}_{6.3}$ active layer showed a significant increase compared to Ag_3BiI_6 active layer. The superior conductivity obtained from the ohmic region in the SCLC plot of $\text{Ag}_3\text{Bi}_{1.1}\text{I}_{6.3}$ active layer (see in Fig. S6) helped carrier transport in an active layer. It resulted in high carrier mobility compared to the control active layer.

The evolution of surface potential of Ag_3BiI_6 and $\text{Ag}_3\text{Bi}_{1.1}\text{I}_{6.3}$ active layers with or without light striking infers clear information about the carrier flows in an entire device. Kelvin Probe Atomic Microscopy (KPFM) helps acquire both the surface morphology and the surface

Table 2

Trap density and mobility for Ag_3BiI_6 ($x=0.0$) and $\text{Ag}_3\text{Bi}_{1.1}\text{I}_{6.3}$ ($x=0.1$) active layers for both the electron-only and the hole-only devices

Active layer	Type of carrier	Trap density (number/cm ³)	Mobility (cm ² /V • s)
Ag_3BiI_6 ($x=0.0$)	electron (n-i-n)	2.28×10^{15}	0.18
	hole (p-i-p)	3.99×10^{14}	24.39
$\text{Ag}_3\text{Bi}_{1.1}\text{I}_{6.3}$ ($x=0.1$)	electron (n-i-n)	2.21×10^{15}	0.37
	hole (p-i-p)	3.63×10^{14}	85.31

potential of an active layer in the dark or under illumination. Fig. 6 (a-1) and (b-1) show the surface morphology of Ag_3BiI_6 and $\text{Ag}_3\text{Bi}_{1.1}\text{I}_{6.3}$ active layers. The averaged surface roughness slightly decreased from 27.6 nm for Ag_3BiI_6 active layer to 23.4 nm for $\text{Ag}_3\text{Bi}_{1.1}\text{I}_{6.3}$ active layer. The results were consistent with the topography from the FE-SEM image, as shown in Fig. 4. Fig. 6 (a-2) and (a-3) show the surface potential measurement at the moment when the light was turned on for Ag_3BiI_6 active layer, and Fig. 6 (b-2) and (b-3) show $\text{Ag}_3\text{Bi}_{1.1}\text{I}_{6.3}$ active layer based on the same measuring condition. The surface potential profiles were summarized in Fig. 6 (a-4) for Ag_3BiI_6 active layer and Fig. 6 (b-4) for $\text{Ag}_3\text{Bi}_{1.1}\text{I}_{6.3}$ active layer. Ag_3BiI_6 active layer showed the same surface potential whether it was in the dark or under illumination. On the other hand, a noticeable surface potential difference was observed when the light struck the target active layer of $\text{Ag}_3\text{Bi}_{1.1}\text{I}_{6.3}$. The minor potential evolution under different conditions elucidated that Ag_3BiI_6 active layer exhibited a low light response than $\text{Ag}_3\text{Bi}_{1.1}\text{I}_{6.3}$ active layer. In addition, the carrier generation in $\text{Ag}_3\text{Bi}_{1.1}\text{I}_{6.3}$ active layer was much more apparent than that in Ag_3BiI_6 active layer when both active layers were illuminated by light. From the microscopic point of view, the superior carrier mobility and the surface potential difference under light illumination of $\text{Ag}_3\text{Bi}_{1.1}\text{I}_{6.3}$ active layer revealed the reason for the improved PCE of the device with $\text{Ag}_3\text{Bi}_{1.1}\text{I}_{6.3}$ active layer from 2.10 % to 2.60%.

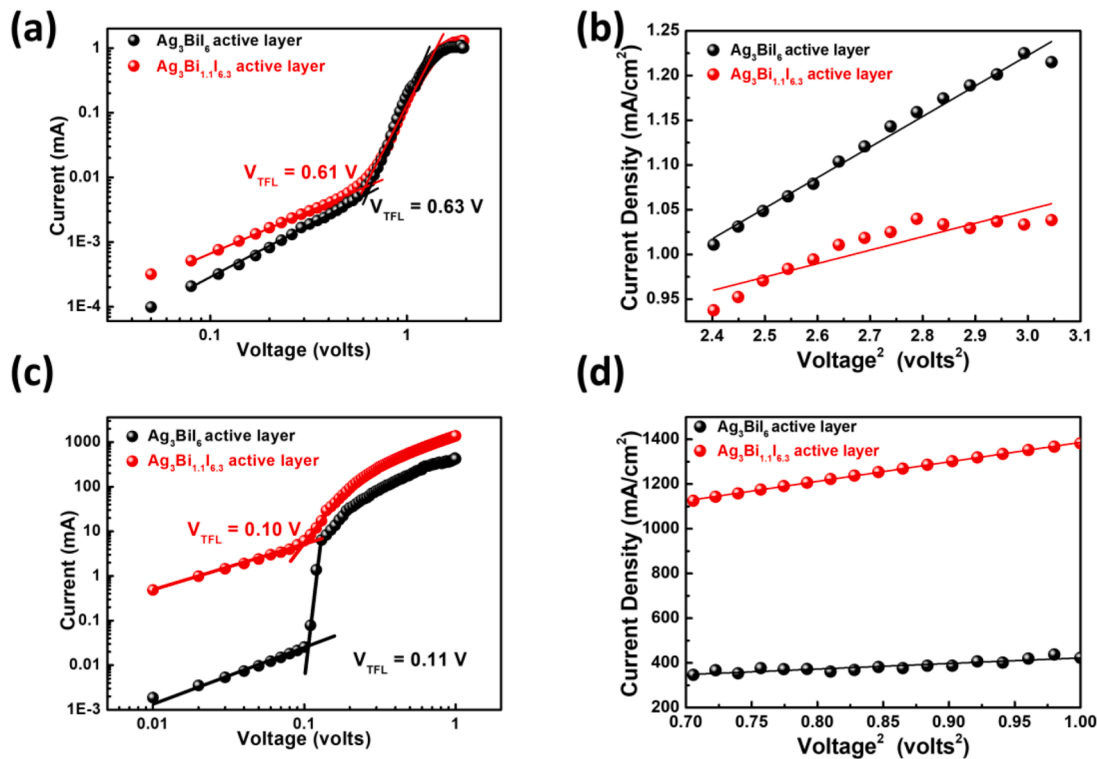


Fig. 5. I - V curves of Ag_3BiI_6 ($x=0.0$) and $\text{Ag}_3\text{Bi}_{1.1}\text{I}_{6.3}$ ($x=0.1$) active layers for the SCLC model fitting: (a) I - V curve and (b) I - V^2 curve at the Child's region for the electron-only devices; (c) I - V curve and (d) I - V^2 curve at the Child's region for the hole-only devices.

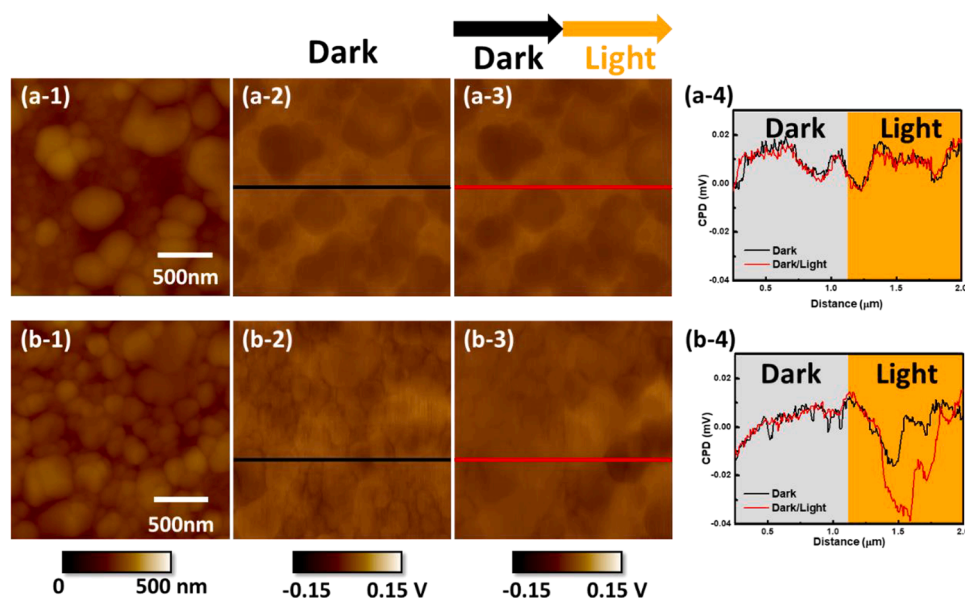


Fig. 6. Morphology and the surface potential mapping of an active layer in the dark or under illumination: (a-1, b-1) topography, (a-2, b-2) the surface potential mapping in the dark, (a-3, b-3) the surface potential mapping transitioning from in the dark to under illumination, and (a-4, b-4) the profile of surface potential mapping in the dark and under illumination for Ag_3BiI_6 (a-1~a-4) and $\text{Ag}_3\text{Bi}_{1.1}\text{I}_{6.3}$ (b-1~b-4).

Moreover, the long-term stability of a device is also a crucial characteristic for evaluating a photovoltaic material. Fig. 7 shows the changing photovoltaic performance of unencapsulated devices with either the control or the target active layer left in the ambient environment. The device with $\text{Ag}_3\text{Bi}_{1.1}\text{I}_{6.3}$ active layer maintained 80% of its initial PCE after 3,000 h. However, the device with Ag_3BiI_6 active layer only maintained 80% of its initial PCE for the first 750 h. The main deterioration of PCE came from the decrease of photocurrent due to the adsorption of gas molecules in the active layer. The adsorbed gas molecules might trap the charge carrier to reach a low free energy condition. [35] It rationally infers that fewer gas molecules were adsorbed in the

device with $\text{Ag}_3\text{Bi}_{1.1}\text{I}_{6.3}$ active layer exhibiting much-compacted morphology than the device with Ag_3BiI_6 active layer when stored in the ambient environment. The smooth path for carrier transportation in the device with $\text{Ag}_3\text{Bi}_{1.1}\text{I}_{6.3}$ active layer can prolong the lifetime of such a device.

Conclusion

This study demonstrates the composition engineering of the silver bismuth iodide active layer. The relationships between the chemical composition and the optoelectrical properties, including energy level,

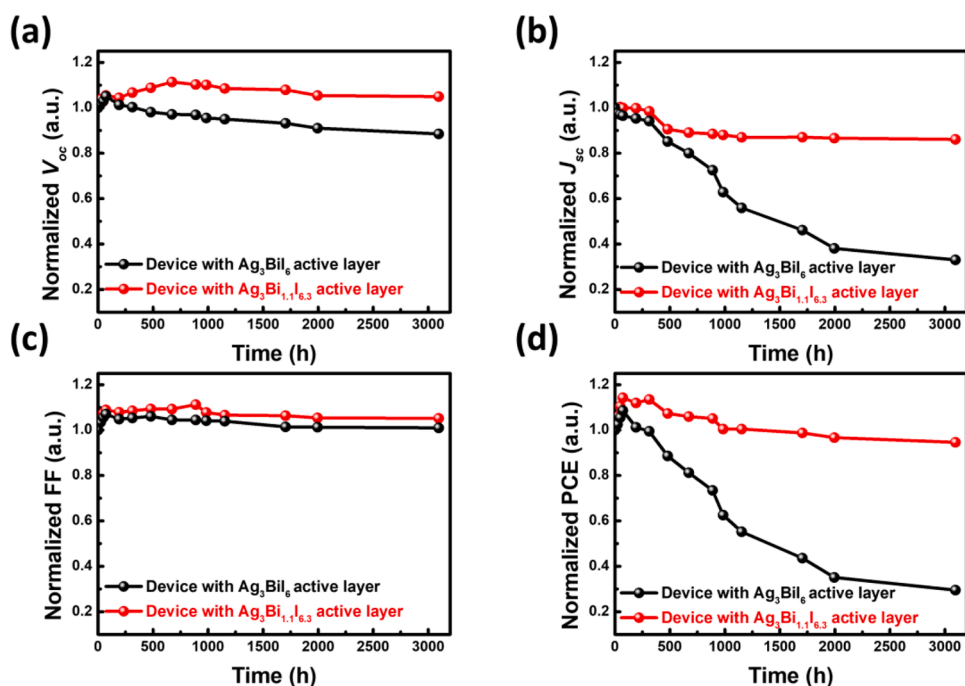


Fig. 7. Stability test of SBI solar cells stored in ambient condition with RH% at around 35%: (a) normalized V_{oc} , (b) normalized J_{sc} , (c) normalized FF, and (d) normalized PCE of devices with Ag_3BiI_6 or $\text{Ag}_3\text{Bi}_{1.1}\text{I}_{6.3}$ active layer.

surface potential evolution, and carrier mobility, were investigated to realize a non-toxic rudorffite solar cell with a PCE of 2.60 %. For the long-term stability test, the device maintained over 80% of its initial PCE after being stored in an ambient environment (RH% at around 35%) for 3,000 h. While decent photovoltaic performance can be obtained from SBI photovoltaics, it shed light on how a non-toxic material with high stability can be obtained. Its non-toxicity, low cost, and stable characteristics make rudorffite solar cells a potential photovoltaic material for a new generation of solar cells.

Experimental section

Material and method

In this study, silver iodide (Alfa Aesar, 99.999%), bismuth iodide (Alfa Aesar, 99.999%), titanium isopropoxide (Sigma-Aldrich, 75 wt% in isopropanol), diisopropoxide bis(acetylacetonate) (Sigma-Aldrich, 75 wt. % in isopropanol), bis(trifluoromethane)sulfonamide lithium (Sigma-Aldrich, 99.95%), tin (II) acetate (Sigma-Aldrich, 99.99%), poly (triaryl amine) (Sigma-Aldrich, Mn=7,000-10,000), dimethyl sulfoxide (ECHO, >99.9%), acetonitrile (Acros, >99.5%), 4-tert-butylpyridine (Sigma-Aldrich, 96%), chlorobenzene (Acros, 99.8%), toluene (ECHO, >99.5%), 2-propanol (STAREK, >99.8%), α -terpineol (C₁₀H₁₈O, Merck, 90%), ethyl cellulose (Acros, ethoxyl content 48%), acetic acid (Acros, 99.99%) were used without any pre-treatment. For the meso-Sn:TiO₂ paste, the synthesizing method followed our previous work, [36] where TiO₂ nanocrystal doped with 1.00 mol% of Sn was prepared with the sol-gel method. 200mL of aqueous dilute acetic acid with a 1:3 volume ratio of acetic acid and D.I. water was prepared. After that, 1.33 mol of tin acetate was dissolved into the as-prepared acetic acid solution. The titanium dioxide precursor was prepared by mixing 50.0 g of titanium isopropoxide and 20 mL of isopropanol. While the as-prepared acetic acid was vigorously stirred and placed in an ice bath, the titanium dioxide precursor was slowly dropped into the stirring acetic acid solution. The mixed solution was kept for 12 h to allow the reaction to complete. The product was collected through centrifugation. The paste with 23 wt % of Sn doped TiO₂ was prepared by mixing 1.0-mol % Sn doped TiO₂, α -terpineol, and ethyl cellulose. To prepare the rudorffite precursors, using Ag₃BiI₆ as an example, 211.3 mg of silver iodide and 176.9 mg of bismuth iodide were weighed and transferred into a 7-mL vial. A milliliter of DMSO was added to the vial to obtain a 0.3 M silver bismuth iodide precursor solution. For poly(triaryl amine) (PTAA) hole transporting layer precursor, 15 mg of PTAA was dissolved into 1 mL of chlorobenzene. Additional 2.5 μ L of Li-TFSI solution, which was prepared by adding 100 mg of Li-TFSI to 0.5 mL of acetonitrile, was added into the as-prepared solution to obtain the PTAA hole transport layer precursor solution.

Device fabrication

The device architecture followed the established mesoporous n-i-p structure, which was reported elsewhere.[36–38] Before the coating process, FTO glasses (7 Ω , FrontMaterials Co. Ltd.) were washed sequentially with deionized water, acetone, and isopropanol to remove and adsorbed organic contaminants. A compacted TiO₂ layer was deposited onto the front side of a clean FTO glass using spray pyrolysis with 0.05 M of titanium diisopropoxide bis(acetylacetonate) solution at 450 °C. The prepared Sn-TiO₂ paste was screen-printed onto the compact layer of TiO₂ followed by calcination at 500°C for half an hour. After the glasses were cooled to room temperature, the as-prepared precursor solution of silver bismuth iodide was deposited on the glass using the anti-solvent assisted crystallization method, where 75 μ L of SBI precursor was deposited using a two-steps spin-coating process. First, the solution was sprayed out for 10s at a low spin rate of 1,000 rpm, followed by a high spin rate of 7,000 rpm for 30s to form a film with the desired thickness of around 300 nm. During the second step of

the spin coating process, around 500 μ L of chlorobenzene was steadily dripped onto the wet film to remove any excess solvent and assist the crystallization of SBI materials. The substrate with SBI film was immediately transferred onto a hotplate at 160°C for 15 min. Subsequently, 50 μ L of Li-TFSI doped PTAA was spin-coated at 3,000 rpm for 30 s onto the SBI layer. Lastly, the device was completed after 120-nm thick silver electrodes with 0.04 mm² active layer were thermal evaporated onto the hole transporting layer.

Characterization

Ultraviolet–visible spectroscopy (UV–Vis) absorption was measured using UV–vis spectrometer (V-730, Jasco). The UPS (Sigma Probe, Thermo VG-Scientific) equipped Hel (21.2 eV) light source was applied to investigate the energy level of the active layers. Controlled Potential Differences (CPD) profile was acquired from a scanning Kelvin probe analyzer equipped with a 2-mm gold tip (KP Technology, SKP 5050). The film morphologies of active layers with various bismuth ratios were acquired using a Field-Emission Scanning Electron Microscope (FE-SEM) (SU-8010, HITACHI) with an accelerating voltage of 10 kV. The *I*–*V* curves of the devices were measured with a digital source meter (2400, Keithley) under simulated solar illumination at 100 mW cm⁻², AM 1.5G standard and with a calibrated Si-reference cell (Bunkokeiki, BS-520BK) with a KG-5 filter. The External Quantum Efficiency (EQE) spectra were recorded using an IPCE spectrometer (EQE-R-3011, Enli Technology Co. Ltd). The surface potential mappings were collected by KPFM (Dimension-3100 Multimode, Digital Instruments) with a Pt/Ir-coated tip in tapping mode under wavelength-switchable LED light source (WLS-LED, Mightex) illuminated at an angle of 45°. The crystal structure and microstructure were analyzed by X-ray Diffraction Pattern (XRD, D2 phaser with Xflash 430, Bruker).

Declaration of Competing Interest

The authors declare that they have no known competing financial interests or personal relationships that could have appeared to influence the work reported in this paper.

Acknowledgments

The authors appreciate Dr. Ming-Tao Lee (BL-13A1) and Dr. Jyh-Fu Lee (BL-17C1) at National Synchrotron Radiation Research Centre for useful discussion and suggestions, and Miss Y.-M. Chang at Instrumentation Centre of National Tsing Hua University for TEM analysis. The authors also thank the Microscopy Center at Chang Gung University for technical assistance. The financial support from Ministry of Science and Technology, Taiwan (Project No. 110-2221-E-182-044, and 110-2628-E-182-001), Chang Gung University (QZRPD181) and Chang Gung Memorial Hospital at Linkou (CMRPD2L0081 and BMRPC74) are highly appreciated.

Supplementary materials

Supplementary material associated with this article can be found, in the online version, at doi:10.1016/j.cej.2022.100275.

References

- [1] A. Liu, K. Liu, H. Zhou, H. Li, X. Qiu, Y. Yang, M. Liu, Solution evaporation processed high quality perovskite films, *Science Bulletin* 63 (2018) 1591–1596.
- [2] M. Xiao, F. Huang, W. Huang, Y. Dkhissi, Y. Zhu, J. Etheridge, A. Gray-Weale, U. Bach, Y.-B. Cheng, L. Spiccia, A Fast Deposition-Crystallization Procedure for Highly Efficient Lead Iodide Perovskite Thin-Film Solar Cells, *Angew. Chem. Int. Ed.* 53 (2014) 9898–9903.
- [3] Q. Jiang, Z. Chu, P. Wang, X. Yang, H. Liu, Y. Wang, Z. Yin, J. Wu, X. Zhang, J. You, Planar-Structure Perovskite Solar Cells with Efficiency beyond 21%, *Adv. Mater.* 29 (2017), 1703852.
- [4] <https://www.nrel.gov/pv/cell-efficiency.html>. 2017.

- [5] J.Y. Kim, J.-W. Lee, H.S. Jung, H. Shin, N.-G. Park, High-Efficiency Perovskite Solar Cells, *Chem. Rev.* 120 (2020) 7867–7918.
- [6] Y. Cheng, H. Li, B. Liu, L. Jiang, M. Liu, H. Huang, J. Yang, J. He, J. Jiang, Vertical 0D-Perovskite/2D-MoS₂ van der Waals Heterojunction Phototransistor for Emulating Photoelectric-Synergistically Classical Pavlovian Conditioning and Neural Coding Dynamics, *Small* 16 (2020), 2005217.
- [7] Y. Zhou, L. Zhao, Z. Ni, S. Xu, J. Zhao, X. Xiao, J. Huang, Heterojunction structures for reduced noise in large-area and sensitive perovskite x-ray detectors, *Sci. Adv.* 7 (2021) eabg6716.
- [8] J. Zhao, L. Zhao, Y. Deng, X. Xiao, Z. Ni, S. Xu, J. Huang, Perovskite-filled membranes for flexible and large-area direct-conversion X-ray detector arrays, *Nat. Photonics* 14 (2020) 612–617.
- [9] M.-C. Yen, C.-J. Lee, K.-H. Liu, Y. Peng, J. Leng, T.-H. Chang, C.-C. Chang, K. Tamada, Y.-J. Lee, All-inorganic perovskite quantum dot light-emitting memories, *Nat. Commun.* 12 (2021) 4460.
- [10] Y. Jiang, L. Qiu, E.J. Juarez-Perez, L.K. Ono, Z. Hu, Z. Liu, Z. Wu, L. Meng, Q. Wang, Y. Qi, Reduction of lead leakage from damaged lead halide perovskite solar modules using self-healing polymer-based encapsulation, *Nat. Energy* 4 (2019) 585–593.
- [11] B. Niu, H. Wu, J. Yin, B. Wang, G. Wu, X. Kong, B. Yan, J. Yao, C.-Z. Li, H. Chen, Mitigating the Lead Leakage of High-Performance Perovskite Solar Cells via In Situ Polymerized Networks, *ACS Energy Lett* 6 (2021) 3443–3449.
- [12] L. Gollino, T. Pauporté, Lead-Less Halide Perovskite Solar Cells, *Sol. RRL* 5 (2021), 2000616.
- [13] M.-C. Wu, Y.-Y. Li, S.-H. Chan, K.-M. Lee, W.-F. Su, Polymer Additives for Morphology Control in High-Performance Lead-Reduced Perovskite Solar Cells, *Sol. RRL* 4 (2020), 2000093.
- [14] S. Shahbazi, M.-Y. Li, A. Fathi, E.W.-G. Diau, Realizing a Cosolvent System for Stable Tin-Based Perovskite Solar Cells Using a Two-Step Deposition Approach, *ACS Energy Lett* 5 (2020) 2508–2511.
- [15] E. Jokar, C.-H. Chien, A. Fathi, M. Rameez, Y.-H. Chang, E.W.-G. Diau, Slow surface passivation and crystal relaxation with additives to improve device performance and durability for tin-based perovskite solar cells, *Energy Environ. Sci.* 11 (2018) 2353–2362.
- [16] C.-M. Tsai, N. Mohanta, C.-Y. Wang, Y.-P. Lin, Y.-W. Yang, C.-L. Wang, C.-H. Hung, E.W.-G. Diau, Formation of Stable Tin Perovskites Co-crystallized with Three Halides for Carbon-Based Mesoscopic Lead-Free Perovskite Solar Cells, *Angew. Chem. Int. Ed.* 56 (2017) 13819–13823.
- [17] F. Hao, C.C. Stoumpos, D.H. Cao, R.P.H. Chang, M.G. Kanatzidis, Lead-free solid-state organic-inorganic halide perovskite solar cells, *Nat. Photonics* 8 (2014) 489–494.
- [18] L. Lanzetta, T. Webb, N. Zibouche, X. Liang, D. Ding, G. Min, R.J.E. Westbrook, B. Gaggio, T.J. Macdonald, M.S. Islam, S.A. Haque, Degradation mechanism of hybrid tin-based perovskite solar cells and the critical role of tin (IV) iodide, *Nat. Commun.* 12 (2021) 2853.
- [19] J. Pascual, G. Nasti, M.H. Aldamasy, J.A. Smith, M. Flatken, N. Phung, D. Di Girolamo, S.-H. Turren-Cruz, M. Li, A. Dallmann, R. Avolio, A. Abate, Origin of Sn (ii) oxidation in tin halide perovskites, *Materials Advances* 1 (2020) 1066–1070.
- [20] T. Mahmoudi, W.-Y. Rho, M. Kohan, Y.H. Im, S. Mathur, Y.-B. Hahn, Suppression of Sn²⁺/Sn⁴⁺ oxidation in tin-based perovskite solar cells with graphene-tin quantum dots composites in active layer, *Nano Energy* 90 (2021), 106495.
- [21] K. Liu, H. Zhou, P. Wang, J. Fang, H. Li, M. Cao, X. Gao, X. Qiu, M. Liu, Bismuth vanadate single crystal particles modified with tungsten for efficient photoelectrochemical water oxidation, *Catal. Today* 335 (2019) 511–519.
- [22] S.M. Jain, T. Edvinsson, J.R. Durrant, Green fabrication of stable lead-free bismuth based perovskite solar cells using a non-toxic solvent, *Commun. Chem.* 2 (2019) 91.
- [23] M. Khazaei, K. Sardashti, C.-C. Chung, J.-P. Sun, H. Zhou, E. Bergmann, W. A. Dunlap-Shohl, Q. Han, I.G. Hill, Jacob L. Jones, D.C. Lupascu, D.B. Mitzi, Dual-source evaporation of silver bismuth iodide films for planar junction solar cells, *J. Mater. Chem. A* 7 (2019) 2095–2105.
- [24] K.W. Jung, M.R. Sohn, H.M. Lee, I.S. Yang, S.D. Sung, J. Kim, E. Wei-Guang Diau, W.I. Lee, Silver bismuth iodides in various compositions as potential Pb-free light absorbers for hybrid solar cells, *Sustain. Energy Fuels* 2 (2018) 294–302.
- [25] I. Turkevych, S. Kazaoui, E. Ito, T. Urano, K. Yamada, H. Tomiyasu, H. Yamagishi, M. Kondo, S. Aramaki, Photovoltaic Rudorffites: Lead-Free Silver Bismuth Halides Alternative to Hybrid Lead Halide Perovskites, *ChemSusChem* 10 (2017) 3754–3759.
- [26] H.C. Sansom, G.F.S. Whitehead, M.S. Dyer, M. Zanella, T.D. Manning, M.J. Pitcher, T.J. Whittles, V.R. Dhanak, J. Alaria, J.B. Claridge, M.J. Rosseinsky, AgBiI₄ as a Lead-Free Solar Absorber with Potential Application in Photovoltaics, *Chem. Mater.* 29 (2017) 1538–1549.
- [27] M.D. Prasad, M.G. Krishna, S.K. Batabyal, Silver Bismuth Iodide Nanomaterials as Lead-Free Perovskite for Visible Light Photodetection, *ACS Appl. Nano Mater.* 4 (2021) 1252–1259.
- [28] Y. Kim, Z. Yang, A. Jain, O. Voznyy, G.-H. Kim, M. Liu, L.N. Quan, F. P. Garcia de Arquer, R. Comin, J.Z. Fan, E.H. Sargent, Pure Cubic-Phase Hybrid Iodobismuthates AgBi₂I₇ for Thin-Film Photovoltaics, *Angew. Chem. Int. Ed.* 55 (2016) 9586–9590.
- [29] B. Ghosh, B. Wu, X. Guo, P.C. Harikesh, R.A. John, T. Baikie, A.T.S. Wee Arramel, C. Guet, T.C. Sum, S. Mhaisalkar, N. Mathews, Superior Performance of Silver Bismuth Iodide Photovoltaics Fabricated via Dynamic Hot-Casting Method under Ambient Conditions, *Adv. Energy Mater.* 8 (2018), 1802051.
- [30] N. Pai, J. Lu, T.R. Gengenbach, A. Seeber, A.S.R. Chesman, L. Jiang, D. C. Senevirathna, P.C. Andrews, U. Bach, Y.-B. Cheng, A.N. Simonov, Silver Bismuth Sulfoiodide Solar Cells: Tuning Optoelectronic Properties by Sulfide Modification for Enhanced Photovoltaic Performance, *Adv. Energy Mater.* 9 (2019), 1803396.
- [31] J.W. Park, Y. Lim, K.-Y. Doh, M.T. Jung, Y.I. Jeon, I.S. Yang, H.-s. Choi, J. Kim, D. Lee, W.I. Lee, Enhancement of the photovoltaic properties of Ag₂BiI₅ by Cu doping, *Sustain. Energy Fuels* 5 (2021) 1439–1447.
- [32] H. Zhu, A. Erbing, H. Wu, G.J. Man, S. Mukherjee, C. Kamal, M.B. Johansson, H. Rensmo, M. Odelius, E.M.J. Johansson, Tuning the Bandgap in Silver Bismuth Iodide Materials by Partly Substituting Bismuth with Antimony for Improved Solar Cell Performance, *ACS Appl. Energy Mater.* 3 (2020) 7372–7382.
- [33] H. Wu, H. Zhu, A. Erbing, M.B. Johansson, S. Mukherjee, G.J. Man, H. Rensmo, M. Odelius, E.M.J. Johansson, Bandgap Tuning of Silver Bismuth Iodide via Controllable Bromide Substitution for Improved Photovoltaic Performance, *ACS Appl. Energy Mater.* 2 (2019) 5356–5362.
- [34] S.B. Cho, J. Gazquez, X. Huang, Y. Myung, P. Banerjee, R. Mishra, Intrinsic point defects and intergrowths in layered bismuth triiodide, *Phys. Rev. Mater.* 2 (2018), 064602.
- [35] N. Aristidou, C. Eames, I. Sanchez-Molina, X. Bu, J. Kosco, M.S. Islam, S.A. Haque, Fast oxygen diffusion and iodide defects mediate oxygen-induced degradation of perovskite solar cells, *Nat. Commun.* 8 (2017) 15218.
- [36] S.-H. Chen, S.-H. Chan, Y.-T. Lin, M.-C. Wu, Enhanced power conversion efficiency of perovskite solar cells based on mesoscopic Ag-doped TiO₂ electron transport layer, *Appl. Surf. Sci.* 469 (2019) 18–26.
- [37] M.-C. Wu, S.-H. Chan, K.-M. Lee, S.-H. Chen, M.-H. Jao, Y.-F. Chen, W.-F. Su, Enhancing the efficiency of perovskite solar cells using mesoscopic zinc-doped TiO₂ as the electron extraction layer through band alignment, *J. Mater. Chem. A* 6 (2018) 16920–16931.
- [38] M.-C. Wu, Y.-Y. Li, S.-H. Chan, K.-M. Lee, W.-F. Su, Polymer Additives for Morphology Control in High-Performance Lead-Reduced Perovskite Solar Cells, *Sol. RRL* 4 (2020), 2070063.